

Photodesorption of acetonitrile CH₃CN in UV-irradiated regions of the Interstellar Medium : an experimental evidence

ROMAIN BASALGÈTE ¹, ANTONIO JESUS OCAÑA ¹, GÉRALDINE FÉRAUD ¹, CLAIRE ROMANZIN,² LAURENT PHILIPPE ¹,
XAVIER MICHAUT ¹, JEAN-HUGUES FILLION ¹ AND MATHIEU BERTIN ¹

¹*Sorbonne Université, Observatoire de Paris, PSL University, CNRS, LERMA, F-75014, Paris, France*

²*Univ Paris Saclay, CNRS UMR 8000, ICP, F-91405, Orsay, France*

ABSTRACT

Pure acetonitrile (CH₃CN) and mixed CO:CH₃CN and H₂O:CH₃CN ices have been irradiated at 15 K with Vacuum UltraViolet (VUV) photons in the 7-13.6 eV range using synchrotron radiation. VUV photodesorption yields of CH₃CN and of photo-products have been derived as a function of the incident photon energy. The coadsorption of CH₃CN with CO and H₂O molecules, which are expected to be among the main constituents of interstellar ices, is found to have no significant influence on the VUV photodesorption spectra of CH₃CN, CHCN•, HCN, CN• and CH₃•. Contrary to what has generally been evidenced for most of the condensed molecules, these findings point toward a desorption process for which the CH₃CN molecule that absorbs the VUV photon is the one desorbing. It can be ejected in the gas phase as intact CH₃CN or in the form of its photo-dissociation fragments. Astrophysical VUV photodesorption yields, applicable to different locations, are derived and can be incorporated into astrochemical modeling. They vary from $0.67(\pm 0.33) \times 10^{-5}$ to $2.0(\pm 1.0) \times 10^{-5}$ molecule/photon for CH₃CN depending on the region considered, which is high compared to other organic molecules such as methanol. These results could explain the multiple detections of gas phase CH₃CN in different regions of the interstellar medium and are well-correlated to astrophysical observations of the Horsehead nebula and of protoplanetary disks (such as TW Hya and HD 163296).

Keywords: UV photodesorption, Interstellar Ices, Acetonitrile, PDR, Protoplanetary disks

1. INTRODUCTION

Acetonitrile (CH₃CN) is a complex organic molecule (COM) regularly detected in several regions of the Interstellar Medium (ISM) at different stages of star formation (Purcell et al. 2006; Bergner et al. 2018; Calcutt et al. 2018; Liszt et al. 2018; Zeng et al. 2018). In the ISM, acetonitrile can be formed both by gas phase reactions and by grain surface chemistry in icy mantles. In protoplanetary disks, pure gas phase chemistry fails to explain the observed abundances of CH₃CN (Öberg et al. 2015; Loomis et al. 2018), indicating that its detection is intimately linked to processes associated with ices. In these disks, CH₃CN detection extends far from the central Young Stellar Object (YSO), in regions where the temperature of the icy mantles is expected to be low enough ($T < 100$ K) so that gas phase CH₃CN should accrete on the surface of the icy dust grains. The presence of CH₃CN in the gas phase therefore implies that a non-thermal process should maintain a sufficient amount of gas phase CH₃CN via desorption from the

surface of ice mantles. UV photodesorption of CH₃CN from ices, which is the desorption induced by the UV irradiation of ices, is so far the most important non-thermal process taken into account in disk modeling. In the case of the Horsehead nebula, for which the separation between the UV-illuminated Photo-Dominated Region (PDR) and the UV-shielded dense core is easily made (Gratier et al. 2013; Guzmán et al. 2014), observations show that CH₃CN gas abundance is 30 times higher in the PDR region than in the dense core. As pure gas phase reactions also fail to explain these abundances, UV photodesorption of CH₃CN from icy mantles is expected to play a major role in PDRs.

Recent experimental investigations on CH₃CN Vacuum UV photodesorption were conducted using an indirect method in the 7-10.2 eV range (Bulak et al. 2020). UV photodesorption of CH₃CN from pure CH₃CN ice was estimated to be $< 7.4 \times 10^{-4}$ molecule desorbed by incident photon. This study is so far the only constraint on the UV photodesorption of CH₃CN from

pure CH_3CN ices. Several experimental studies regarding UV photodesorption of simple molecules such as CO , CO_2 , N_2 or CH_4 (Bertin et al. 2013; Fillion et al. 2014; Carrascosa et al. 2019; Dupuy et al. 2017) and more complex molecules such as CH_3OH and H_2CO (Bertin et al. 2016; Martín-Doménech et al. 2016; Féraud et al. 2019) have shown that UV photodesorption yields are strongly dependent on the ice composition: e.g., when diluted in CO -dominated ices, CH_3OH UV photodesorption is quenched whereas H_2CO UV photodesorption is enhanced, compared to the case of pure CH_3OH and H_2CO ice respectively. This indicates that the UV photodesorption of complex molecules should be systematically studied as a function of the ice composition. This is even more relevant when considering that pure ices of organics are not likely to be found in the ISM. However, the exact role played by the ice composition is still difficult to predict a priori. We thus propose to provide absolute photodesorption yields in composite ices where the molecule to study is embedded in a CO or H_2O icy matrix. Those two kinds of ices can serve as models of the realistic icy mantles that could be found in the ISM, mainly composed of water, but which can also present a CO -rich phase in denser regions beyond the CO snowlines (Pontoppidan, K. M. et al. 2003; Boogert et al. 2015).

In the present study, we quantify the Vacuum UV (VUV) photodesorption, in the 7-13.6 eV range, of CH_3CN from pure CH_3CN ice and from CH_3CN mixed with or on top of CO and H_2O ices. VUV photodesorption yields of photo-products are also derived. The yields are obtained as a function of the incident VUV photon energy, which allows to discuss the physical mechanisms at play. Absolute VUV photodesorption yields applicable to astronomically relevant environments are also provided in order to be incorporated into astrochemical modeling. In Sect.2, the experimental procedure is presented. In Sect.3, the results and their astrophysical implications are discussed.

2. METHODS

Experiments are conducted at the DESIRS beamline of the SOLEIL synchrotron facility (Nahon et al. 2012). The setting used on this beamline provides VUV photons in the energy range of 7 - 14 eV with a ~ 1 eV bandwidth. The photon flux, measured with a calibrated silicon photodiode, depends on the photon energy. It varies from 6.3×10^{14} photon. s^{-1} at 7 eV to 6.4×10^{13} photon. s^{-1} at 14 eV. The beamline is equipped with a rare gas filter to suppress higher energy harmonics from the undulator. The SPICES setup

(Surface Processes and ICES) is connected to the synchrotron beamline to run the experiments. It consists of an ultra-high vacuum chamber (base pressure $\sim 10^{-10}$ mbar) within which a rotatable copper substrate (polycrystalline oxygen-free high-conductivity copper) can be cooled down to $T \sim 15$ K by a closed-cycle helium cryostat. A tube positioned a few millimeters away from the substrate allows to inject a partial pressure of gas phase molecules that will stick on the cold substrate, thus forming the molecular ices. During this process, the base pressure of the chamber is not significantly modified. The gaseous molecules used during these experiments were acetonitrile CH_3CN (99.8% purity, Sigma-Aldrich), carbon monoxide CO (Air Liquide, 99.9%) and water H_2O (liquid chromatography standard, Fluka). Liquid products (H_2O and CH_3CN) were further purified using several freeze-pump-thaw cycles. To form the mixed ices ($\text{CO}:\text{CH}_3\text{CN}$ and $\text{H}_2\text{O}:\text{CH}_3\text{CN}$), the corresponding gaseous mixture is prepared in a gas-introduction system equipped with a capacitive pressure gauge before introduction into the experiment.

The ice thickness is expressed in monolayer (ML), roughly equivalent to a molecule surface density of 10^{15} molecules. cm^{-2} . Prior to the synchrotron experiments, the temperature-programmed desorption (TPD) technique is used to calibrate the ice thickness. This calibration allows us to control the number of ML deposited onto the substrate with a relative precision of about 10 % (Bertin et al. 2017). Pure CH_3CN ices (~ 60 ML) and mixed $\text{CO}:\text{CH}_3\text{CN}$ (~ 100 ML) ices were formed at 15 K. Mixed $\text{H}_2\text{O}:\text{CH}_3\text{CN}$ ices (~ 100 ML) were formed at 100 K and cooled down to 15 K before irradiation to ensure that the resulting water ice is in its compact amorphous phase. This phase is commonly referred to as compact amorphous solid water (c-ASW). 1 ML of CH_3CN was also deposited on pure CO ice (~ 30 ML) at 15 K and on pure H_2O ice (~ 30 ML) at 100 K, followed by a cooling down to 15 K.

The VUV beam is sent at a 45° incidence on the ice surface on a spot of ~ 1 cm^2 . While the ices are irradiated, the photodesorption of neutral species is monitored by recording the desorbed molecules in the gas phase using a quadripolar mass spectrometer (QMS) equipped with an electron-impact ionization chamber at 70 eV. Each gas-phase species is probed by monitoring the mass signal of its corresponding intact cation. Typical desorption signals (raw data) are shown in the Appendix A. At the end of the irradiation procedure, TPD experiments (from 15 K to 200 K with a ramp of 12 K. min^{-1}) are performed to evaporate all molecules

from the substrate before a new ice is formed. These TPD experiments have also been used to investigate any photochemistry (see Appendix B). The photodesorption yields presented in this article (in molecule/desorbed per incident photon, displayed as molecule/photon for more simplicity in the following) are derived from the raw desorption signals given by the QMS on the considered mass channel. A detailed explanation is provided in the Appendix A. The mixture ratios used for the mixed ices were chosen to progressively study the impact of the dilution of CH₃CN in CO or H₂O ices on the photodesorption yields but may not be representative of the interstellar ice analogs that could be found in the ISM.

3. RESULTS AND DISCUSSION

3.1. *Pure acetonitrile ice*

In Figure 1, we present the VUV photodesorption spectra derived from our experiments on pure CH₃CN ices and we also compare these spectra with the VUV absorption spectrum (in the 7 - 11.2 eV range) of pure CH₃CN ice at 10 K from Sivaraman et al. 2016. The attribution of photo-products to the mass channels is discussed in the following. The VUV photodesorption of masses 15 and 26 is attributed to CH₃• and CN• respectively, which are expected to be direct UV photo-dissociation product of CH₃CN. This is consistent with the UV photo-dissociation of gas phase acetonitrile for which C-C bond breaking is observed (Moriyama et al. 1998; Kanda et al. 1999). HCN and CH₄ are observed as major photo-products in VUV photolysis experiments of pure CH₃CN ice at 20 K (Bulak et al. 2021) and 12 K (Hudson & Moore 2004). Accordingly, we attributed the masses 16 and 27 to CH₄ and HCN photodesorption respectively. HCN was also proposed as a possible direct UV photo-dissociation product of CH₃CN in gas phase by Schwell et al. 2008. We assumed that the mass 39 corresponds to CHCN• photodesorption. Based on gas phase experiments for which H-loss reaction is assumed to occur for the UV photo-dissociation of CH₃CN (Moriyama et al. 1998; Schwell et al. 2008), the detection of CHCN• in our experiment could be expected to come from dehydrogenation of CH₃CN induced by VUV photo-absorption. A raw photodesorption signal was detected on the mass 40, which could correspond to the desorption of CH₂CN•. However, when considering the fragmentation of the mass 41 (CH₃CN) into the mass 40 (CH₂CN•) in the ionization chamber of our QMS, the corrected signal on the mass 40 falls below our detection limit so that we can only provide an upper limit of $\sim 1 \times 10^{-6}$ molecule/photon for the VUV photodesorption yield of CH₂CN• from pure acetonitrile ices (this is also the case for the binary mixed ices in

Section 3.2).

Additionally, Hudson & Moore 2004 has observed the isomerization of CH₃CN into CH₃NC during VUV irradiation (with an hydrogen lamp) of pure CH₃CN ice at 12 K. This isomerization was detected by infrared via the -N≡C stretching mode at 2170 cm⁻¹. From Hudson & Moore 2004, we could expect to have only a few percent of CH₃CN isomerization during our irradiation experiments and we did not observe the -N≡C stretching mode by infrared on pure CH₃CN ices (this is also the case for the binary mixed ices in Section 3.2). Therefore, we made the assumption that the VUV photodesorption of the mass 41 in our experiments is dominated by CH₃CN desorption rather than CH₃NC. The isomerization of HCN into HNC was not observed by Hudson & Moore 2004 and accordingly, we estimated that the VUV photodesorption of the mass 27 in our experiments is dominated by HCN desorption and not its isomer HNC.

The mass 30 was attributed to C₂H₆ desorption, assumed to originate from radical-radical reaction between CH₃• molecules, based on low-energy electron irradiation experiments of pure CH₃CN ices (Ipolyi et al. 2007; Bass et al. 2012). The mass 28 is the most desorbing one in our experiments. It could be attributed to N₂, H₂CN and/or C₂H₄ VUV photodesorption. Post-irradiation TPD experiments have also revealed a mass 28 desorption features which peaks below 40 K, and intensity of which increases with the total irradiation fluence; and not observed on non-irradiated ices (see Figure 5 in the Appendix B). This indicates that the irradiation also implies the accumulation of the associated species onto the ice during irradiation. Among all the possible candidates at the origin of the mass 28 channel, the low desorption temperatures points toward its association with N₂ (sub)monolayer desorption (Collings et al. 2004; Smith et al. 2016). Accordingly, we assumed that the photodesorption of the mass 28 from pure CH₃CN ice was dominated by N₂. The formation of N₂ might result from photochemistry involving CN•* which is left in electronically excited states (A²Π, B²Σ⁺) after dissociation of CH₃CN according to gas phase experiments (Schwell et al. 2008).

The VUV photodesorption spectra of the species presented in Figure 1 have the same dependence in energy: the photodesorption efficiency is increasing from 7 to 10-10.5 eV and seems to be constant above 10.5 eV. The small variations above this energy are significantly lower than the error bars, and cannot be confidently consid-

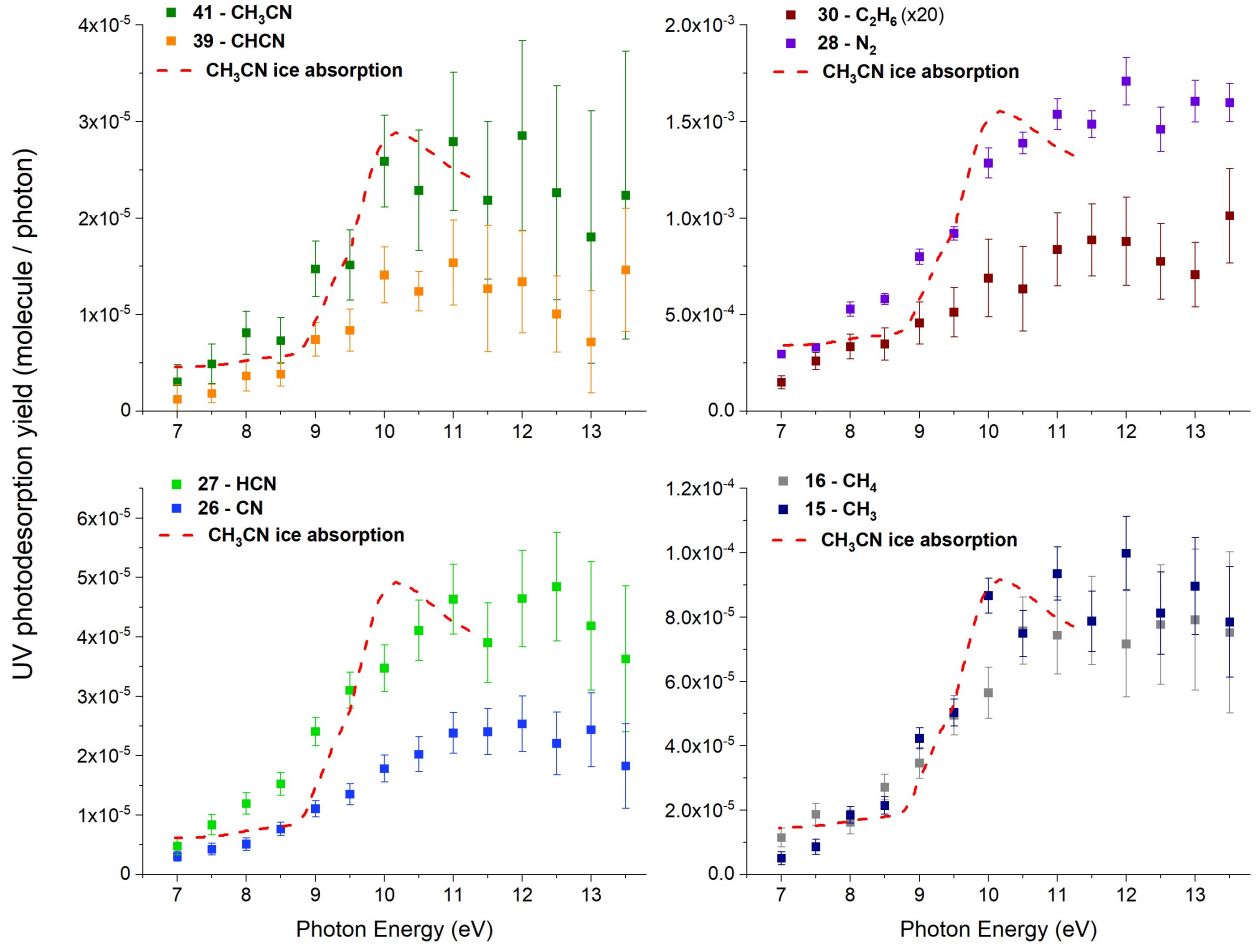


Figure 1. VUV photodesorption spectra (squares with error bars), as a function of the incident photon energy, of CH_3CN (mass 41), CHCN (mass 39), C_2H_6 (mass 30), N_2 (mass 28), HCN (mass 27), CN (mass 26), CH_4 (mass 16) and CH_3 (mass 15) from pure CH_3CN ice at 15 K. Each mass channel is corrected from the cracking of higher masses fragmentation in the mass spectrometer. The attribution of species to the mass channels is discussed in Sect.3.1. In each panel, we also displayed in red dashed lines the VUV absorption spectrum of CH_3CN ice at 10 K (in arbitrary units) from Sivaraman et al. 2016.

ered as a "real" modification of the photodesorption yields. In Figure 1, we can also see that there is a good correlation between the VUV absorption spectrum of CH_3CN ice and the VUV photodesorption spectra of the different molecules presented. The similarities between these spectra indicates that the photodesorption of these species originates from the same phenomena, which is the VUV absorption of CH_3CN in condensed phase. Concerning the photodesorption efficiencies, they range from $\sim 1.2 \times 10^{-5}$ molecule/photon for CHCN to $\sim 1.6 \times 10^{-3}$ molecule/photon for N_2 , around 10.5 eV. Finally, the VUV photodesorption yield of intact CH_3CN is $\sim 2.5 \times 10^{-5}$ molecule/photon at 10.5 eV. Our results compare very well to the recent study of Bulak et al. 2020 who could not measure directly the photodesorption yield of CH_3CN from pure CH_3CN ice but

provided an upper limit of 7.4×10^{-4} molecule/photon, compatible with our measurements.

3.2. Binary ices

In Figure 2, we summed up our results on CH_3CN , HCN and CN photodesorption from the binary ices tested : mixed $\text{CH}_3\text{CN}:\text{CO}$ ice, mixed $\text{CH}_3\text{CN}:\text{H}_2\text{O}$ ice and layered ices (~ 1 ML of CH_3CN on top of pure CO and on top of pure H_2O ice). For the specific case of CH_3CN photodesorption from a mixed $\text{CH}_3\text{CN}:\text{CO}$ (1:7) ice, the yields above 10.5 eV are not shown for more visibility because of the large error bars. In addition to the presented molecules in Figure 2, we searched for the desorption of masses 42, 43, 45 and 52 which could correspond to CNO , HCNO , NH_2CHO (formamide) and C_2N_2 respectively. However, the signals on these channels were too noisy to derive a photodesorption yield and we can only provide an upper limit of 5×10^{-6}

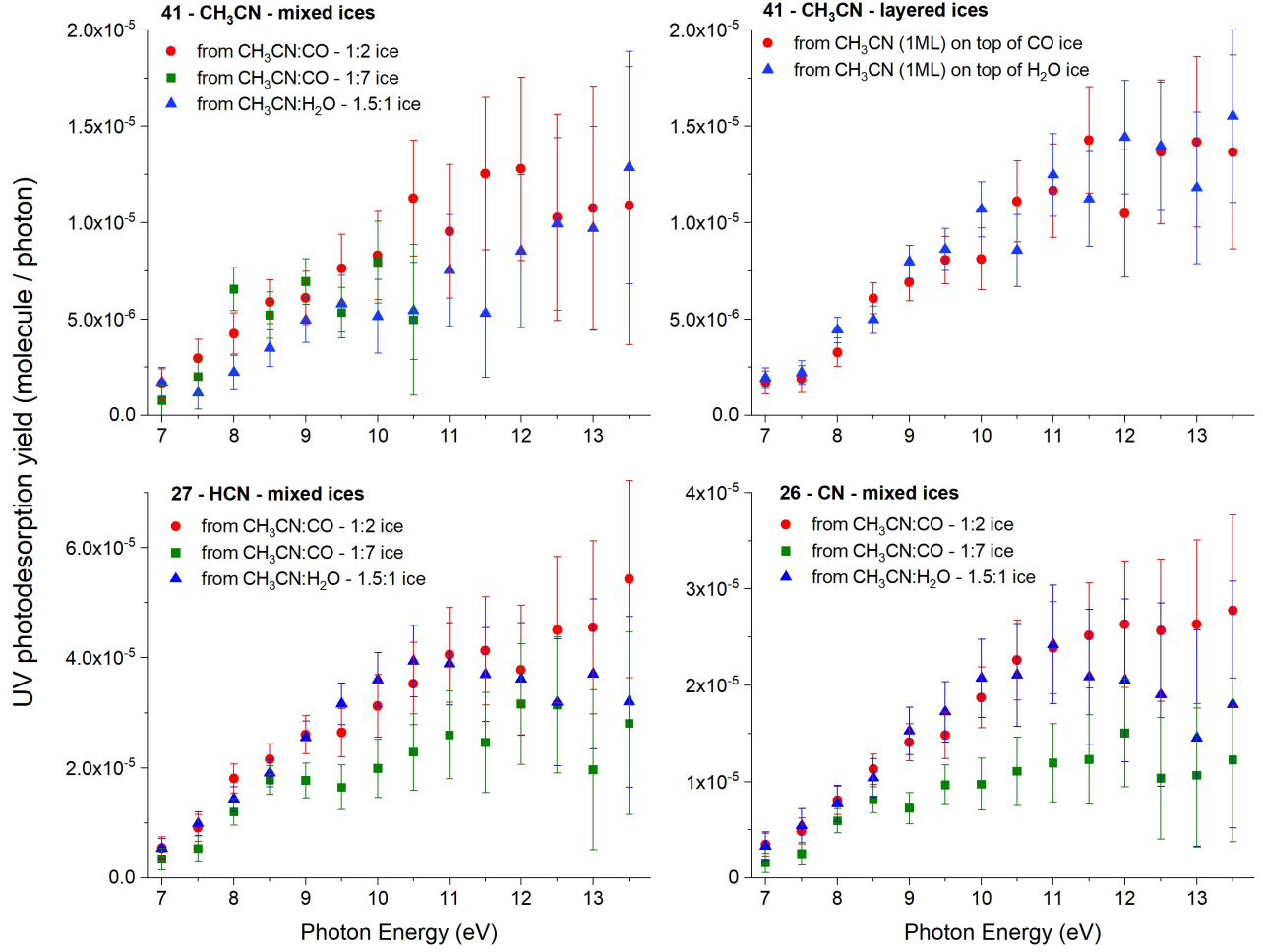


Figure 2. VUV photodesorption spectra, as a function of the incident photon energy, of CH₃CN (mass 41) from mixed CH₃CN:CO and mixed CH₃CN:H₂O ices (top left panel) and from 1 ML of CH₃CN on top of CO and on top of H₂O ice (top right panel). VUV photodesorption of HCN (mass 27) and CN (mass 26) from mixed CH₃CN:CO and CH₃CN:H₂O ices are presented in the bottom panels. These yields were derived for ices at 15 K.

molecule/photon for these masses. The photodesorption data for the masses 30, 28 and 16 in the case of the mixed ices are displayed in the Appendix C in Figure 7. The desorption signals for the masses 30 and 28 are significantly higher in the case of mixed CH₃CN:CO ices compared to the case of mixed CH₃CN:H₂O ice. This is due to a contribution of CO photodesorption for the mass signal 28 and most probably H₂CO and/or NO photodesorption for the mass signal 30 in the case of mixed CH₃CN:CO ices. The desorption signal on the mass 16 is not significantly dependent on the presence of CO or H₂O molecules in the ice but a possible contribution of atomic O photodesorption to this mass signal prevents us from precisely quantifying a possible VUV photodesorption of CH₄ from the mixed ices.

We do not observe a significant influence of the pres-

ence of H₂O and CO molecules on the shape of the VUV photodesorption spectra for the presented molecules in Figure 2 (CH₃CN, HCN, CN●). A similar behaviour is observed for the masses 15 and 39 which can be unambiguously attributed to CH₃● and CHCN● (see Figure 6 in the Appendix C). In similar experiments, indirect desorption mechanisms have been observed in the case of simpler molecules such as N₂ or CH₄ deposited on top of pure CO ice (Bertin et al. 2013; Dupuy et al. 2017), "pre-irradiated" pure CO₂ ice (Fillion et al. 2014) or N₂, CO, Kr and Ar on top of pure water c-ASW ice (Dupuy et al. 2021). In these cases, the desorption of one molecule is induced by the UV photo-absorption of another one whose excited state relaxation induces an energy transfer to the desorbing molecule. Experimentally, this results in similarities between the VUV photodesorption spectrum of the molecule considered

and the VUV absorption spectrum of CO or H₂O in condensed phase. In the case of more complex molecules, such as CH₃OH, this indirect mechanism was not observed (Bertin et al. 2016). In our CH₃CN experiments, the VUV photodesorption spectra of CH₃CN, CHCN•, HCN, CH₃• and CN• from the mixed and layered ices do not show any similarities with the UV absorption profile of CO or H₂O molecules in condensed phase. These data are compared for the case of CH₃CN UV photodesorption from the layered ices in Figure 3. It is however surprising to observe that the VUV photodesorption yields of CH₃CN from CO-dominated ices are similar (when considering the error bars) between the 1:2 and 1:7 ratios (see Figure 2, upper left panel). As CH₃CN is more diluted in the CH₃CN:CO - 1:7 ice, we would have expected to obtain a lower yield compared to the case of the CH₃CN:CO - 1:2 ice. The fact that there is no clear signature of the CO UV absorption spectrum between 7.5 and 9.5 eV in the photodesorption spectrum of CH₃CN from CH₃CN (1 ML) on top of CO ice (see Figure 3) seems to exclude the possibility of a significant indirect desorption mechanism induced by CO molecules when the CH₃CN surface concentration is high. However, for higher dilution of CH₃CN in a CO environment, a desorption of CH₃CN triggered by the excitation of the CO matrix cannot be totally ruled out. The similarities of the photodesorption yields of CH₃CN from CO-dominated ices for the 1:2 and the 1:7 ratios could also be explained by less bounded CH₃CN molecules in CO-dominated ices but this point would need additional experiments in lower concentration regimes to conclude. Finally, an indirect desorption mechanism induced by CO or H₂O molecules does not seem to be at play or significant in our set of experiments for the desorption of the molecules cited above (CH₃CN, CHCN•, HCN, CH₃• and CN•) from CH₃CN-containing ices.

The absolute values of the VUV photodesorption yields of CH₃CN, CHCN•, HCN, CH₃• and CN• from the binary mixed ices are slightly diminished compared to the case of pure CH₃CN ice but this effect is not significant when considering the error bars and could be explained by a lower number of CH₃CN molecules available for desorption at the ice surface, inducing a lower desorption flux in the case of mixed ices. The deposition technique (mixed ices or layered ices) does not have a significative influence on the VUV photodesorption of these molecules either. The photodesorption yields of CH₃CN from 1 ML of CH₃CN on top of CO or H₂O ice are about half of that from pure CH₃CN ice, which could be due to the fact that several CH₃CN-containing lay-

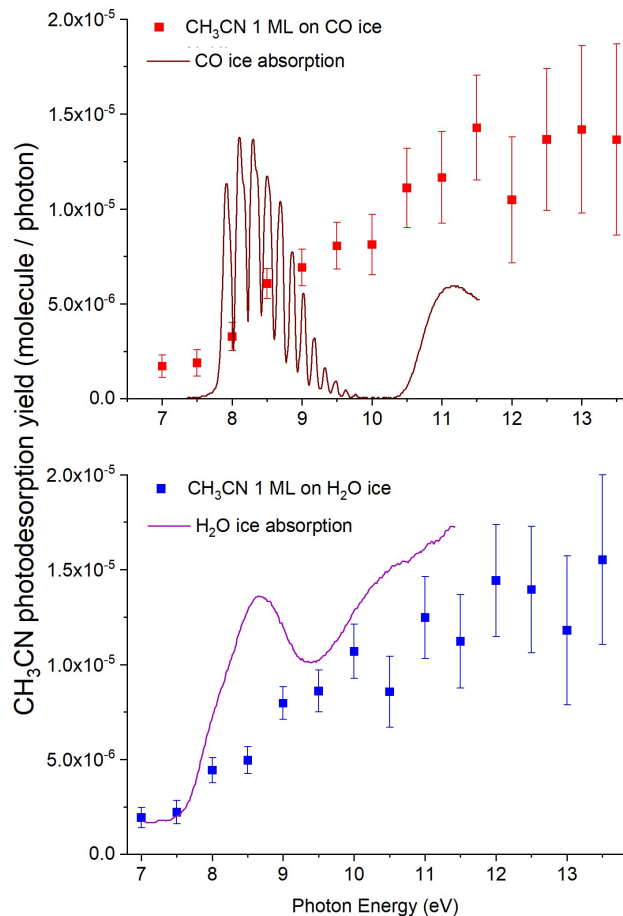


Figure 3. Top panel: comparison of CH₃CN VUV photodesorption spectrum from a layered CH₃CN (1 ML) on top of CO ice with the VUV absorption spectrum of CO in condensed phase (from Lu et al. 2005). Bottom panel: comparison of CH₃CN VUV photodesorption spectrum from a layered CH₃CN (1 ML) on top of H₂O ice with the VUV absorption spectrum of H₂O in condensed phase (from Lu et al. 2008). The VUV absorption spectrum of CO and H₂O in condensed phase are shown in arbitrary units.

ers are involved in the desorption of CH₃CN from pure CH₃CN ice. It is much likely that the VUV photodesorption of CH₃CN, CHCN•, HCN, CH₃• and CN• from the ices tested (pure, mixed and layered ices) occurs via a process for which the CH₃CN molecule that absorbs the VUV photon is the one desorbing. It can be ejected as intact CH₃CN or in the form of its photo-dissociation fragments. The desorption of CH₃CN may involve dissociation and exothermic recombination of the excited molecule. According to our results, this process seems to be independent of the presence of CO or H₂O molecules surrounding the VUV absorbing CH₃CN molecule in the ice.

3.3. Astrophysical implications

By integrating our experimental photodesorption spectra with UV spectra that are representative of the UV fields found in different regions of the ISM, we are able to provide photodesorption yields that are suitable for astrophysical environments. The UV field used were: the UV emission spectra of a classical T Tauri Star representative of protoplanetary disks (France et al. 2014), the UV field produced by cosmic-ray secondary electrons representative of dense interstellar clouds (Gredel et al. 1987) and the UV interstellar radiation field (ISRF) from Mathis et al. (1983). The resulting yields are presented in Table 1 and can be incorporated in astrochemical modeling. As discussed previously, we found that the VUV photodesorption of CH₃CN and what is associated with its photo-fragments (CHCN•, HCN, CN• and CH₃•) does not strongly depend on the presence of CO or H₂O molecules in the ice, which are expected to be among the main constituents of ices in the ISM (Boogert et al. 2015). Accordingly, we took the photodesorption spectra from pure CH₃CN ice (Figure 1) to derive the yields presented in Table 1, which are thus assumed to be applicable to any CO or H₂O dominated ices containing CH₃CN molecules. The yields corresponding to protoplanetary disks and dense interstellar clouds are found to be identical within the error bars and are approximatively equal to the experimental yields at the Lyman α around 10.2 eV (Figure 1), as it is the energy that dominates the UV field in these regions. The yields corresponding to the ISRF are found to be lower due to a higher contribution of the UV field at low energy (< 10 eV) where photodesorption is less efficient. Interestingly, the desorption of CH₃CN and its photo-fragments are found in the same order of magnitude in the region considered. The desorption of the masses 30, 28 and 16 from the mixed ices will not be discussed in this section as it is not possible to clearly attribute species to these mass channels (see Sect.3.2). Moreover, the formation of the associated species (N₂, C₂H₆, CH₄) has much likely involved the absorption of at least 2 VUV photons, in a limited time and spatial interval for the resulting radicals to react. This makes their possible experimental desorption not astrophysically relevant when considering the very low UV flux observed in the discussed regions of the ISM compared to our experimental UV flux.

As stated in the Introduction, the astrophysical observations of gas phase acetonitrile CH₃CN and of gas phase methanol CH₃OH in the Horsehead UV-illuminated PDR and UV-shielded dense core region show that UV photodesorption of these molecules from

Table 1. Astrophysical photodesorption yield ($\times 10^{-5}$ molecule/photon) extrapolated from our experimental results on pure CH₃CN ices at 15 K, for different astrophysical environments

Photodesorbed species	ISRF ^(a)	Dense Clouds ^(b) and Disks ^(c)
CH ₃ CN	0.67 \pm 0.33	2.0 \pm 1.0
CHCN	0.34 \pm 0.17	1.0 \pm 0.5
HCN	1.1 \pm 0.6	3.3 \pm 1.7
CN	0.60 \pm 0.30	1.7 \pm 0.9
CH ₃	2.1 \pm 1.0	6.5 \pm 3.3

NOTE—(a) UV field from Mathis et al. (1983). (b) UV field from Gredel et al. (1987). (c) UV field from France et al. (2014)

icy grains should play a significant role (Gratier et al. 2013; Guzmán et al. 2014). A quantitative comparison of CH₃OH and CH₃CN abundances in this region is to be put in contrast with our experimental results. According to Gratier et al. 2013 and Guzmán et al. 2014, CH₃OH abundances are found to be similar between the PDR and the dense core region whereas CH₃CN is 30 times more abundant in the PDR than in the dense core region. In the PDR, CH₃OH is found to be less abundant than CH₃CN by approximatively one order of magnitude. Among the possible mechanisms that could explain these observations, our experiments clearly point toward a higher quantitative role of CH₃CN VUV photodesorption compared to the case of CH₃OH VUV photodesorption. In fact, we found that VUV photodesorption of CH₃CN is not significantly dependent on the ice composition and is above 10^{-5} molecule/photon whereas, in similar experiments (Bertin et al. 2016), CH₃OH VUV photodesorption is not detected when methanol is mixed with CO ice (only an upper limit of 10^{-6} molecule/photon has been derived). The higher VUV absorption cross section of CH₃CN compared to CH₃OH (based on gas phase absorption cross sections; Cheng et al. 2002, Schwell et al. 2008) along with the resilience of nitriles to UV photolysis, which has been demonstrated in the case of acetonitrile versus acetic acid in pure ices at 15 K (Bernstein et al. 2004), could be an interesting route to explain these experimental results.

Our experimental results may also explain the astrophysical observations of gas phase CH₃CN and CH₃OH in protoplanetary disks. In the case of the protoplane-

tary disk around the T Tauri star TW Hya, gas phase abundances of CH₃CN and CH₃OH are found to be similar (Walsh et al. 2016; Loomis et al. 2018) whereas in the case of the disk around the Herbig Ae star HD 163296, CH₃CN is strongly detected and CH₃OH emission lines are below the detection limits (Bergner et al. 2018; Carney et al. 2019). As suggested in Bergner et al. 2018, Herbig Ae stars are expected to be stronger UV emitters than T Tauri stars. Therefore, the role of VUV photodesorption of CH₃CN and CH₃OH from interstellar ices has been raised by Bergner et al. 2018 as a possible candidate to explain these differences in the observations of these COMs in protoplanetary disks. Our experimental results, that show a higher VUV photodesorption efficiency of CH₃CN from interstellar ice analogs, by at least one order of magnitude, compared to that of CH₃OH, clearly support the assumption of Bergner et al. 2018. However, the VUV photodesorption yields of COMs used in disk modeling are often higher than the experimental ones (e.g., Loomis et al. 2018 considered a CH₃CN VUV photodesorption yield of 10⁻³ molecule/photon in their modeling of the TW Hya disk) and other processes may be of importance to explain the detection of gaseous COMs in these regions (Dupuy et al. 2018; Dartois et al. 2019; Ciaravella et al. 2020; Basalgète et al. 2021a,b).

In this experimental study, we derived a CH₃CN VUV

photodesorption yield of $\sim 2.5 \times 10^{-5}$ molecule/photon at 10.5 eV. This photodesorption was observed to be independent of the presence of CO and H₂O molecules in the ice, which are expected to be among the main constituents of interstellar ices. Interestingly, CH₃CN VUV photodesorption is found to be more efficient than CH₃OH VUV photodesorption (Bertin et al. 2016) by at least one order of magnitude. This shows that the VUV photodesorption of organics from interstellar ices cannot be so far extrapolated from the specific case of one organic molecule. The results obtained from our experiments could participate into explaining the multiple detections of CH₃CN in UV-irradiated regions of the ISM, especially in the case of protoplanetary disks (Loomis et al. 2018; Bergner et al. 2018) and in the case of the Horsehead Nebulae (Gratier et al. 2013; Guzmán et al. 2014).

- 1 This work was done with financial support from (i)
- 2 the Region Ile-de-France DIM-ACAV+ program, (ii)
- 3 the Sorbonne Université "Emergence" program, (iii) the
- 4 ANR PIXyES project, grant ANR-20-CE30-0018 of the
- 5 French "Agence Nationale de la Recherche" and (iv) the
- 6 Programme National "Physique et Chimie du Milieu Inter-
- 7 stellaire" (PCMI) of CNRS/INSU with INC/INP co-
- 8 funded by CEA and CNES. We would like to acknowl-
- 9 edge SOLEIL for provision of synchrotron radiation fa-
- 10 cilities under Project Nos. 20191298, and we gratefully
- 11 thank L. Nahon for his help on the DESIRS beamline.

REFERENCES

- Basalgète, R., Dupuy, R., Féraud, G., et al. 2021a, *Astronomy & Astrophysics*, 647, A35
- Basalgète, R., Dupuy, R., Féraud, G., et al. 2021b, *Astronomy & Astrophysics*, 647, A36
- Bass, A. D., Bredehöft, J. H., Böhler, E., Sanche, L., & Swiderek, P. 2012, *The European Physical Journal D*, 66, 53
- Öberg, K. I., Guzmán, V. V., Furuya, K., et al. 2015, *Nature*, 520, 198
- Bergner, J. B., Guzmán, V. G., Öberg, K. I., Loomis, R. A., & Pegues, J. 2018, *The Astrophysical Journal*, 857, 69
- Bernstein, M. P., Ashbourn, S. F. M., Sandford, S. A., & Allamandola, L. J. 2004, *The Astrophysical Journal*, 601, 365
- Bertin, M., Doronin, M., Fillion, J.-H., et al. 2017, *Astronomy & Astrophysics*, 598, A18
- Bertin, M., Fayolle, E. C., Romanzin, C., et al. 2013, *The Astrophysical Journal*, 779, 120
- Bertin, M., Romanzin, C., Doronin, M., et al. 2016, *The Astrophysical Journal*, 817, L12
- Boogert, A. A., Gerakines, P. A., & Whittet, D. C. 2015, *Annual Review of Astronomy and Astrophysics*, 53, 541
- Bulak, M., Paardekooper, D., Fedoseev, G., & Linnartz, H. 2021, *Astronomy & Astrophysics*, A82, 647
- Bulak, M., Paardekooper, D. M., Fedoseev, G., & Linnartz, H. 2020, *Astronomy & Astrophysics*, 636, A32
- Calcutt, H., Fiechter, M. R., Willis, E. R., et al. 2018, *Astronomy & Astrophysics*, 617, A95
- Carney, M. T., Hogerheijde, M. R., Guzmán, V. V., et al. 2019, *Astronomy & Astrophysics*, 623, A124
- Carrascosa, H., Hsiao, L. C., Sie, N. E., Muñoz Caro, G. M., & Chen, Y. J. 2019, *Monthly Notices of the Royal Astronomical Society*, 486, 1985
- Chatham, H., Hils, D., Robertson, R., & Gallagher, A. 1984, *The Journal of Chemical Physics*, 81, 1770
- Cheng, B.-M., Bahou, M., Chen, W.-C., et al. 2002, *The Journal of Chemical Physics*, 117, 1633

- Ciaravella, A., Muñoz Caro, G. M., Jiménez-Escobar, A., et al. 2020, *Proceedings of the National Academy of Sciences*, 202005225
- Collings, M. P., Anderson, M. A., Chen, R., et al. 2004, *Monthly Notices of the Royal Astronomical Society*, 354, 1133
- Dartois, E., Chabot, M., Id Barkach, T., et al. 2019, *Astronomy & Astrophysics*, 627, A55
- Dupuy, R., Bertin, M., Féraud, G., et al. 2021, *Phys. Rev. Lett.*, 126, 156001
- Dupuy, R., Bertin, M., Féraud, G., et al. 2018, *Nature Astronomy*, 2, 796
- Dupuy, R., Bertin, M., Féraud, G., et al. 2017, *Astronomy & Astrophysics*, 603, A61
- Fayolle, E. C., Bertin, M., Romanzin, C., et al. 2011, *The Astrophysical Journal*, 739, L36
- Fillion, J.-H., Fayolle, E. C., Michaut, X., et al. 2014, *Faraday Discussions*, 168, 533
- France, K., Schindhelm, E., Bergin, E. A., Roueff, E., & Abgrall, H. 2014, *The Astrophysical Journal*, 784, 127
- Féraud, G., Bertin, M., Romanzin, C., et al. 2019, *ACS Earth and Space Chemistry*, 3, 1135
- Gratier, P., Pety, J., Guzmán, V., et al. 2013, *Astronomy & Astrophysics*, 557, A101
- Gredel, R., Lepp, S., & Dalgarno, A. 1987, *ApJL*, 323, L137
- Guzmán, V. V., Pety, J., Gratier, P., et al. 2014, *Faraday Discuss.*, 168, 103
- Hudson, R. & Moore, M. 2004, *Icarus*, 172, 466
- Ipolyi, I., Michaelis, W., & Swiderek, P. 2007, *Phys. Chem. Chem. Phys.*, 9, 180
- Kanda, K., Nagata, T., & Ibuki, T. 1999, *Chemical Physics*, 243, 89
- Liszt, H., Gerin, M., Beasley, A., & Pety, J. 2018, *The Astrophysical Journal*, 856, 151
- Loomis, R. A., Cleaves, L. I., Öberg, K. I., et al. 2018, *The Astrophysical Journal*, 859, 131
- Lu, H.-C., Chen, H.-K., Cheng, B.-M., Kuo, Y.-P., & Ogilvie, J. F. 2005, *Journal of Physics B: Atomic, Molecular and Optical Physics*, 38, 3693
- Lu, H.-C., Chen, H.-K., Cheng, B.-M., & Ogilvie, J. 2008, *Spectrochimica Acta Part A: Molecular and Biomolecular Spectroscopy*, 71, 1485
- Martín-Doménech, R., Muñoz Caro, G. M., & Cruz-Díaz, G. A. 2016, *Astronomy & Astrophysics*, 589, A107
- Mathis, J. S., Mezger, P. G., & Panagia, N. 1983, *A&A*, 500, 259
- Moriyama, M., Tsutsui, Y., & Honma, K. 1998, *The Journal of Chemical Physics*, 108, 6215
- Nahon, L., de Oliveira, N., Garcia, G. A., et al. 2012, *Journal of Synchrotron Radiation*, 19, 508
- Pandya, S. H., Shelat, F. A., Joshipura, K., & Vaishnav, B. G. 2012, *International Journal of Mass Spectrometry*, 323-324, 28
- Pontoppidan, K. M., Fraser, H. J., Dartois, E., et al. 2003, *A&A*, 408, 981
- Purcell, C. R., Balasubramanyam, R., Burton, M. G., et al. 2006, *Monthly Notices of the Royal Astronomical Society*, 367, 553
- Schwell, M., Jochims, H.-W., Baumgärtel, H., & Leach, S. 2008, *Chemical Physics*, 344, 164
- Sivaraman, B., Pavithra, S., Lo, J.-I., et al. 2016, *The Astrophysical Journal*, 825, 141
- Smith, R. S., May, R. A., & Kay, B. D. 2016, *The Journal of Physical Chemistry B*, 120, 1979
- Straub, H. C., Renault, P., Lindsay, B. G., Smith, K. A., & Stebbings, R. F. 1996, *Physical Review A*, 54, 2146
- Tarnovsky, V., Levin, A., Deutsch, H., & Becker, K. 1996, *Journal of Physics B: Atomic, Molecular and Optical Physics*, 29, 139
- Tian, C. & Vidal, C. R. 1998, *Journal of Physics B: Atomic, Molecular and Optical Physics*, 31, 895
- Walsh, C., Loomis, R. A., Öberg, K. I., et al. 2016, *The Astrophysical Journal*, 823, L10
- Zeng, S., Jiménez-Serra, I., Rivilla, V. M., et al. 2018, *Monthly Notices of the Royal Astronomical Society*, 478, 2962
- Zhou, W., Wilkinson, L., Lee, J. W. L., Heathcote, D., & Vallance, C. 2019, *Molecular Physics*, 117, 3066

APPENDIX

A. DERIVATION OF THE VUV
PHOTODESORPTION YIELDS AND
DETERMINATION OF THE ERROR BARS

The photodesorption yields presented in this article (in molecule desorbed per incident photon, displayed as molecule/photon for more simplicity) are derived from the raw desorption signals given by the QMS on the considered mass channel, using the following formula :

$$\Gamma_X(E) = k_X \times \frac{I_X(E)}{\phi(E)} \quad (\text{A1})$$

where X is the neutral species associated with the mass channel considered, E is the photon energy, $\Gamma_X(E)$ is the photodesorption yield of X at E , $I_X(E)$ is the current given by the QMS for the considered mass channel during the irradiation at E , $\phi(E)$ is the photon flux at E and k_X is a proportionality factor between the molecular desorption flux and the QMS signal. The ices studied in this article were sequentially irradiated during a few seconds at several fixed energies while the desorbing mass are continuously recorded by the QMS. Examples of typical signals obtained from the QMS are shown in Figure 4 where the sudden increase and decrease of the mass signals are associated with the opening (irradiation) and closing (background) of the beamline shutter respectively. For each photon energy and each species, $I_X(E)$ is derived by computing the height of the mass signal with respect to the background level for the irradiation step considered. For molecules that could originate from the cracking of their desorbing parent molecules in the ionization chamber of the QMS, I_X is corrected accordingly by using the cracking patterns available on the National Institute of Standards and Technology (NIST) chemistry Webbook.

The proportionality factor k_X in equation A1 is first calibrated using the photodesorption of CO (k_{CO}): a VUV photodesorption spectrum of CO from pure CO ice is obtained by irradiating a pure CO ice (30 ML) previously grown at 15 K in the experiment and it is compared to a reference VUV photodesorption spectrum obtained at higher spectral resolution (Fayolle et al. 2011). k_{CO} is deduced by matching the two spectra after taking into account the ~ 1 eV width of the photon energy profile used in the present study. The proportionality factors corresponding to neutral species other than CO are then computed by taking into account the differences in electron-impact ionization cross sections and apparatus functions of the mass filter,

resulting in the following formula :

$$k_X = \frac{\sigma(CO^+/CO)}{\sigma(X^+/X)} \times \frac{AF(X)}{AF(CO)} \times k_{CO} \quad (\text{A2})$$

where $AF(X)$ is the apparatus function of our QMS for the given species X and $\sigma(X^+/X)$ is the non-dissociative electron-impact ionization cross section for the X neutral species. These cross sections are taken at 70 eV and are available in the literature for CH₃CN (Zhou et al. 2019), C₂H₆ (Chatham et al. 1984), N₂ (Straub et al. 1996), HCN and CN (Pandya et al. 2012), CH₄ (Tian & Vidal 1998) and CH₃ (Tarnovsky et al. 1996). Due to the absence of available data, the non-dissociative electron-impact ionization cross section of radical CHCN, $\sigma(CHCN^+/CHCN)$ was assumed to be equal to the one of CH₃CN, $\sigma(CH_3CN^+/CH_3CN)$. The apparatus function $AF(X)$ describes the transmission of the quadripolar mass filter in the QMS for a fragment with a given mass m , and thus participates, together with the ionization cross section, to the detection efficiency of a given species. For our instrument, the apparatus function has been measured and follows a power law: $AF(X) = (m/28)^{(1.77)}$.

The uncertainty associated with $I_X(E)$, $\delta I_X(E)$, depends on the signal-to-noise ratio and is estimated as the sum of the half-height of the signal noise in the background, and on the top of each peak for the corresponding irradiation step (see Figure 4). The error bars associated with the photodesorption yields for each energy and each species, $\delta \Gamma_X(E)$, and displayed in Figures 1, 2 and 3 are derived from the following equation:

$$\delta \Gamma_X(E) = k_X \times \frac{\delta I_X(E)}{\phi(E)} \quad (\text{A3})$$

Equation A3 results in experimental error bars which depend on the photon energy. Consequently, these error bars are usually larger at high energy due to a lower photon flux. Finally, these error bars only reflect the quality of the recorded signals and do not take into account the uncertainty associated with the calibration of k_X , which is systemic. This uncertainty is not impacting the shape of the UV photodesorption spectra but only the uncertainty on the absolute values of the photodesorption yields. It mainly depends on the uncertainties associated with the apparatus function of the QMS and on the ionization cross sections $\sigma(X^+/X)$. We estimate this uncertainty to be in the order of magnitude of 50% relative to the measured photodesorption yields.

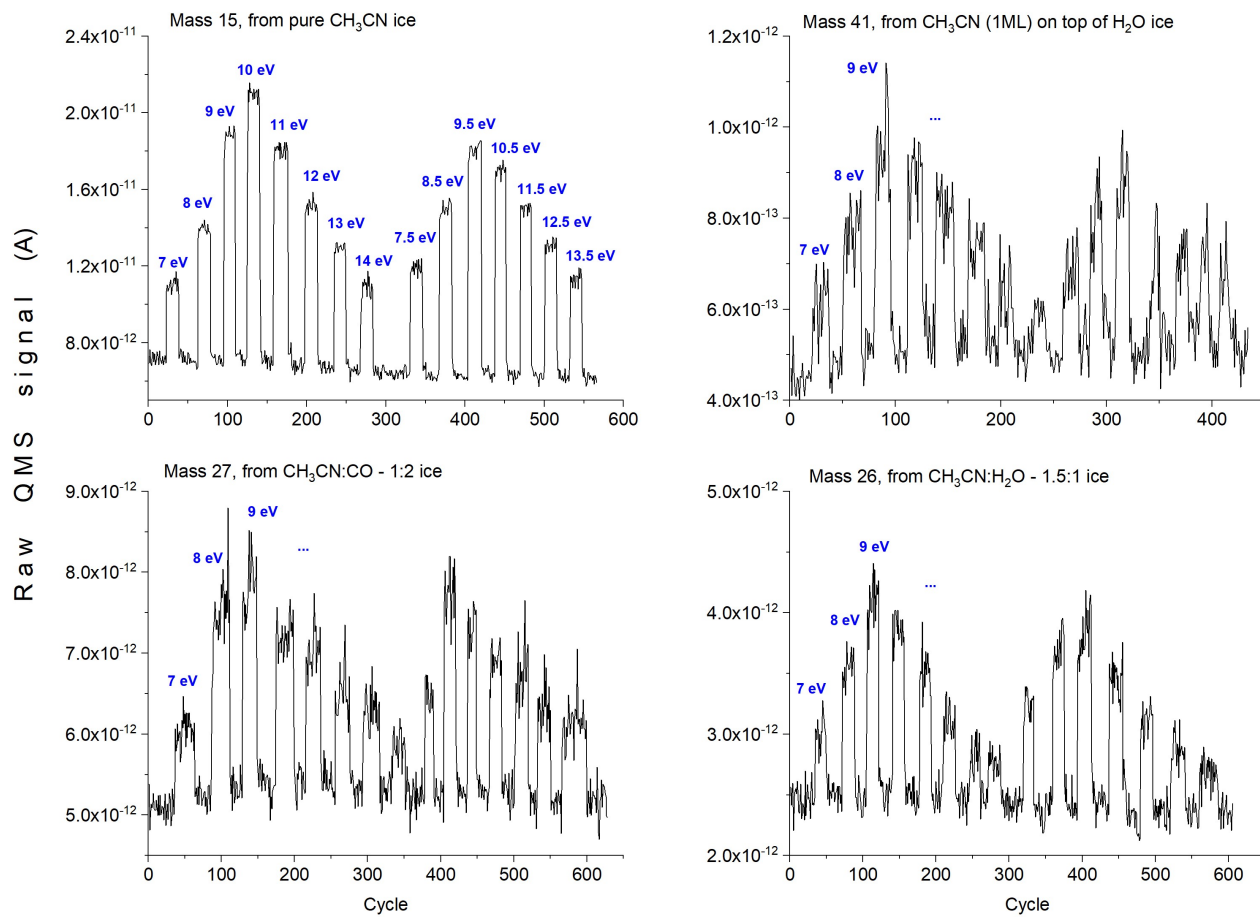


Figure 4. Examples of raw QMS signal observed during irradiation experiments for different mass channels and different ices tested at 15 K. In blue is displayed the incident photon energy used for each irradiation step.

B. ATTRIBUTION OF THE DESORBING MASS 28 CHANNEL USING TPD

As stated in the main text, each studied ices, after one or several irradiations, i.e. energy scans between 7 and 14 eV, were further probed using the Temperature Programmed Desorption (TPD) technique. To this end, the ices were warmed-up using a constant heating rate of 12 K/min, and the desorbed species were detected concomitantly using mass spectrometry. TPD has been in particular used in order to identify the origin of the mass channel 28 detected during photodesorption. Figure 5 presents several TPD curves associated with the mass channel 28 performed from irradiated CH_3CN ices. As one can see from these curves, the majority of the desorption occurs below 40 K, with an onset of desorption at around 25-27 K. Such a low temperature desorption is usually characteristic of the desorption of very volatile species, and match very well the thermal desorption of a small quantity of N_2 deposited onto metallic substrates or water ice substrates (see e.g. work from Collings et al. 2004 and Smith et al. 2016). The other feature observed at higher temperature is in fact associated to the desorption of N_2 trapped into the CH_3CN bulk, which is suddenly released when the ice is sublimated.

Since the 28 signal desorption rises with the irradiation fluence, we attributed this TPD feature to the accumulation of N_2 onto or into the ice during the irradiation. And thus we believe that the photodesorbed mass 28 signal should also be due to some N_2 desorption subsequent to its formation. It should be noted however that TPD is not in itself sufficient to be categorical on this attribution, since, for instance, C_2H_4 could also contribute to this mass 28 signal, even if it should be observed at slightly higher temperature. Finally, any possible uncontrolled pollution by another species, such as CO, has been ruled-out by (i) blank experiments, (ii) the correlation with the photon fluence, and (iii) the fact that no CO vibration could have been detected using in-situ infrared spectroscopy on the irradiated samples. The mass signal 14 was not monitored during the TPD experiments, which prevents us from definitively concluding on the origin of the mass 28 thanks to a possible fragmentation of N_2 into N. A mass signal 14 was however detected during photodesorption experiments but it was high enough so that the possible fragmentation of N_2 into N in the ionization chamber of our QMS has no significative impact on its amplitude, which also prevents us from definitively concluding. The photodesorption of this mass 14 is therefore due to either CH_2 radical or atomic N photodesorption.

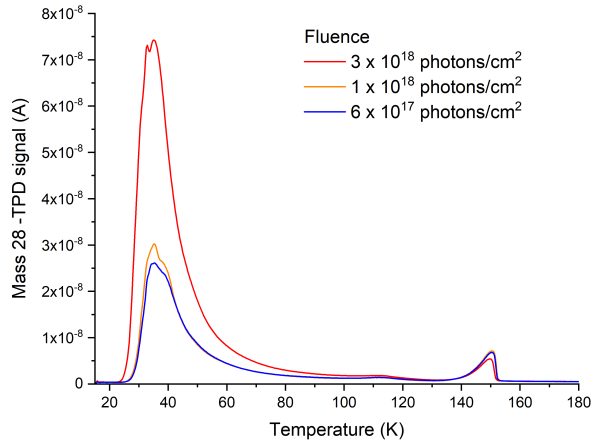


Figure 5. TPD signal on the mass 28 from pure CH_3CN ices as a function of the temperature after its irradiation by successive energy scans between 7 and 14 eV. The fluence received by the ice before TPD is also displayed. The TPD curves were recorded using a constant heating rate of 12 K/min.

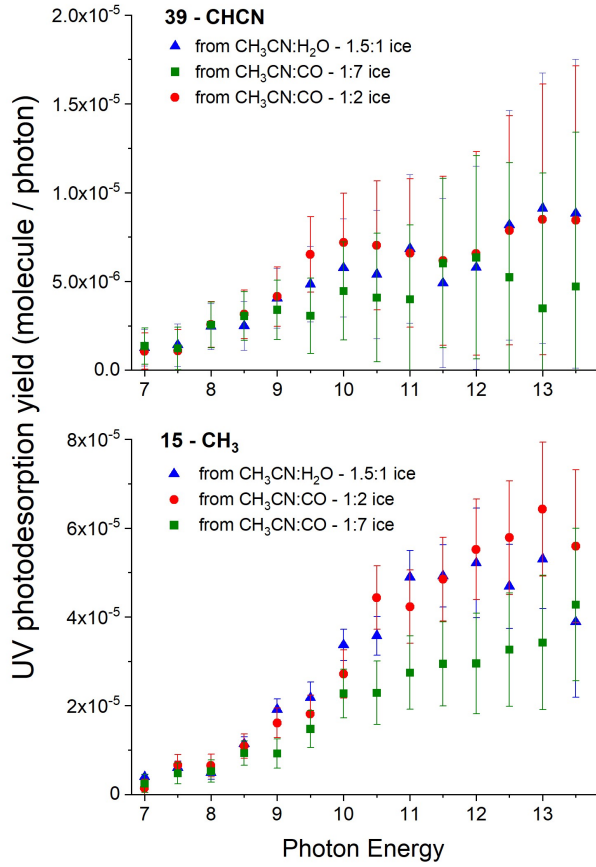
C. UV PHOTODESORPTION YIELDS OF MASSES
 39, 30, 28, 16 AND 15 FROM BINARY ICES AT
 15 K


Figure 6. VUV photodesorption spectra, as a function of the incident photon energy, of CHCN• (mass 39) and CH₃• (mass 15) from mixed CH₃CN:CO and mixed CH₃CN:H₂O ices.

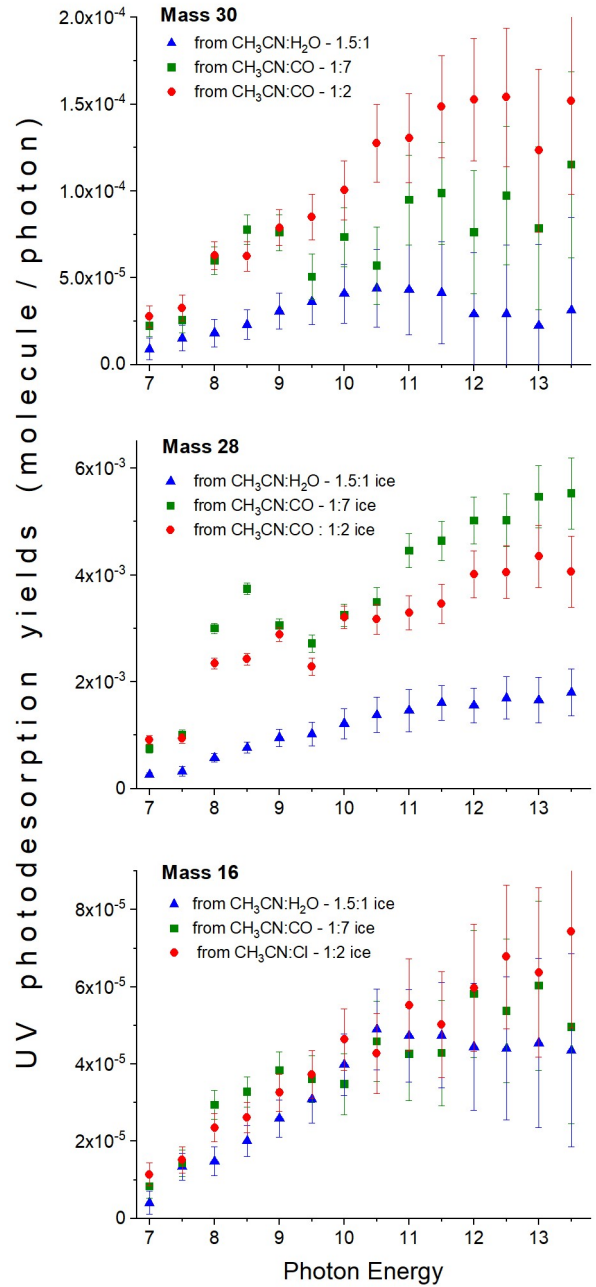


Figure 7. VUV photodesorption spectra, as a function of the incident photon energy, of masses 30, 28 and 16 from mixed CH₃CN:CO and mixed CH₃CN:H₂O ices. The attribution of species to these mass channels is not possible. This is discussed in Sec. 3.2.